J Artif Organs (2011) 14:348–356
DOI 10.1007/s10047-011-0581-9

ORIGINAL ARTICLE

Development of microporous self-expanding stent grafts for treating cerebral aneurysms: designing micropores to control intimal hyperplasia

Shogo Nishi · Yasuhide Nakayama · Hatsue Ishibashi-Ueda · Yoshihiro Okamoto · Masato Yoshida

Received: 24 February 2011 / Accepted: 1 June 2011 / Published online: 23 June 2011

Abstract Treatment of large (diameter 12–25 mm) or giant (diameter >25 mm) cerebral aneurysms with a broad neck in the cranio-cervical area is difficult and carries relatively high risks, even with surgical and/or endovascular methods. To this end, we have been developing a high-performance, self-expanding stent graft which consists of a commercially available NiTi stent (diameter 5 mm, length 20 mm) initially covered with a thin microporous segmented polyurethane membrane fabricated by the dip-coating method. Micropores are then created by the excimer laser ablation technique, and the outer surface is coated with argatroban. There are 2 types of micropore patterns: circular-shaped pore type (pore: diameter 100 μm, opening ratio 12.6%) and the bale-shaped pore type (pore: size 100 × 268 μm, opening ratio 23.6%). This self-expanding stent graft was tested on side-wall aneurysms of both canine carotid arteries that were experimentally induced using the venous pouches from the external jugular veins, with the self-expanding stent graft on one side and a bare self-expanding stent on the other side. All carotid arteries were patent and free of marked stenosis after 1 month. All aneurysms were occluded by stent grafts, while patent in those treated with bare stents. Histologically, the stent grafts with bale-shaped micropores and a high opening ratio were associated with less intimal hyperplasia (187 ± 98 μm) than the bare stents (341 ± 146 μm) or the stent grafts with circular micropores and a low opening ratio (441 ± 129 μm). A pore ratio of 23.6% was found to control intimal growth.

Keywords Self-expanding stent graft · Experimental aneurysm · Embolization · Micropore design · Covered stent

This work was presented in part at the 48th annual meeting of the Japanese Society for Artificial Organs in Sendai.

S. Nishi (✉)
Department of Neurosurgery, Interventional Neurosurgery, and Spinal Surgery, Sapporo-Higashi Tokushukai Hospital, 14-3-1 Higashi, N33, Higashi-ku, Sapporo, Hokkaido 065-0033, Japan
e-mail: nishi@higashi-tokushukai.or.jp

S. Nishi · Y. Nakayama (✉)
Division of Medical Engineering and Materials, National Cerebral and Cardiovascular Center Research Institute, Suita, Osaka, Japan
e-mail: nakayama@ri.ncvc.go.jp

H. Ishibashi-Ueda
Department of Pathology, National Cerebral and Cardiovascular Center, Suita, Osaka, Japan

Y. Okamoto
Chemical Products Division, Development Department, Bridgestone Co., Yokohama, Kanagawa, Japan

M. Yoshida
Department of Neurosurgery, Nozaki Tokushukai Hospital, Osaka, Japan

Introduction

One advantage of stent grafts over vascular stents is the sealing effect of the polymeric cover material, which limits the ingrowth of cellular elements (inhibition of neointimal hyperplasia) and thereby increases patency [1]. Most stent grafts have a synthetic cover made of poly(ethylene terephthalate) (PET), poly(tetrafluoroethylene) (PTFE), or segmented poly(urethane) (SPU) [2]. To avoid in-stent stenosis due to excessive neointimal growth and thrombosis, the

implantation procedure, stent design, and surface structure of the graft can all be manipulated. Ideally, in selecting synthetic coatings for stent grafts, porosity and water permeability should be optimal to obtain patency. For the embolization of large (diameter 12–25 mm) or giant (diameter >25 mm) cerebral aneurysms, we have been developing a high-performance stent graft, which has three significant characteristics, i.e., a thin and expandable SPU membrane, micropores created by the excimer laser ablation technique, and a drug delivery system at the membrane [3].

We have recently tested the effectiveness of this stent graft by treating experimental canine aneurysms [4]. The graft was easily applied to the experimental aneurysm neck and achieved complete occlusion of the aneurysms. Two micropore patterns have been designed for the covering membrane. In the study reported here, we compared the occlusive effects and control of intimal hyperplasia in canine experimental aneurysms of these two stent graft designs.

Materials and methods

Fabrication of stent grafts

The first step in preparing our self-expanding stent graft is to coat bare metal self-expanding stents (Luminexx stents: diameter 5 mm, length 20 mm; Bard Inc, Murray Hill, NJ) with a film of SPU (Miractran, Tokyo, Japan) by dipping them, mounted on a stainless mold (diameter 5 mm), in a tetrahydrofuran solution. The thickness of the cover film is restricted to approximately 50 μm. Micropores are then made in the cover film using a KrF excimer laser apparatus (L4500; Hamamatsu Photonics, Shizuoka, Japan). There are 2 pore designs (Fig. 1): circular-shaped pore type, with a pore diameter and interpore distance of 100 and 250 μm, respectively, to achieve a low opening ratio of 12.6%; bale-shaped pore type, with a pore size and interpore distance of 100 × 268 μm and 250 μm, respectively, to achieve a high opening ratio of 23.6%. In this study, the control was a bare stent with an opening ratio of 86%. The outer surface of the film of the microporous stent grafts is coated with argatroban (500 $\mu g/cm^2$), which is applied using a methanol solution (1% w/v); the solvent is subsequently volatilized for physical adsorption. The fabricated self-expanding stent graft is then remounted on the delivery system (6 or 7 Fr; Bard Inc/Medicon, Setauket, NY).

Preparation of aneurysms in dogs

All animal experiments were performed in the acute setting under clean conditions in compliance with the Principles of Laboratory Animal Care (formulated by the National Society for Medical Research, Chicago, IL) and the Guide for the Care and Use of Laboratory Animals (NIH publication no. 86-23, revised 1985; National Institutes of Health, Bethesda, MD). The research protocol (no. 09043) was approved by the ethics committee of the National Cerebral and Cardiovascular Center Research Institute.

Experimental sidewall carotid aneurysms were created in the bilateral carotid arteries of 6 female beagles (weighing 13–15 kg) by end-to-side anastomosis using an autologous venous pouch, as described in our previous publications [3, 4]. The aneurysms were approximately 5 mm in diameter at the neck and approximately 10 mm in length. All procedures were performed under general anesthesia. The beagles were transmuscularly premedicated with ketamine chloride (dose varied from 150 mg/3 ml to 250 mg/5 ml per beagle), intubated endotracheally, and anesthetized with an intravenous administration of sodium pentobarbital at 50 mg/1 ml or 100 mg/2 ml according to active motion. The bilateral carotid arteries and right external jugular vein were exposed under sterile conditions, and two venous pouches were created by one-sided ligation with threads after harvesting of the right external jugular vein. The carotid artery and the venous pouch were anastomosed (side-to-end anastomosis) with discontinuous 7-0 nylon sutures, while the artery was temporarily clamped. After clamp removal, bleeding was controlled by additional suturing or local compression. Each of the 6 dogs had 1 aneurysm on each carotid artery (except for 1 dog in which a single aneurysm was created). The necks of the aneurysms were marked with X-ray unpenetrated strings. After recovery from anesthesia, the dogs were allowed ad libitum access to food.

Stenting

One month after aneurysm creation, the aneurysms were placed with the prepared stent grafts ($n = 3$ for low opening ratio, $n = 3$ for large opening ratio) and bare stents ($n = 5$). The dogs were administered an antiplatelet agent (clopidogrel 25 mg/day) transorally 3 days prior to stenting, and again 1 month after stenting. The procedure was performed under general anesthesia. A 7 Fr short sheath was inserted into the right femoral artery. The 7 Fr delivery system, including the stent graft or bare stent, was entered into the sheath, navigated into the affected carotid artery, and positioned across the neck of the aneurysm under fluoroscopy. The self-expanding stent graft or bare stent was then released at this site. Angiography was subsequently performed to confirm the states of treated aneurysms. All dogs recovered from anesthesia without complications.

Angiography and histological study

Angiography was performed 1 month after stenting. Histological examination was performed after euthanasia, using a

cross-sectional sample from the stented portion of the aneurysm.

Statistical analysis

Intimal thickness measured at 8 points, every 45° in the transverse section, was analyzed using the Student *t* test.

Results

Stenting

Self-expanding stent grafts with two different micropore designs were fabricated (Fig. 1). The micropores were prepared uniformly over the film (Fig. 1b, e). The stent struts were completely embedded within the cover film,

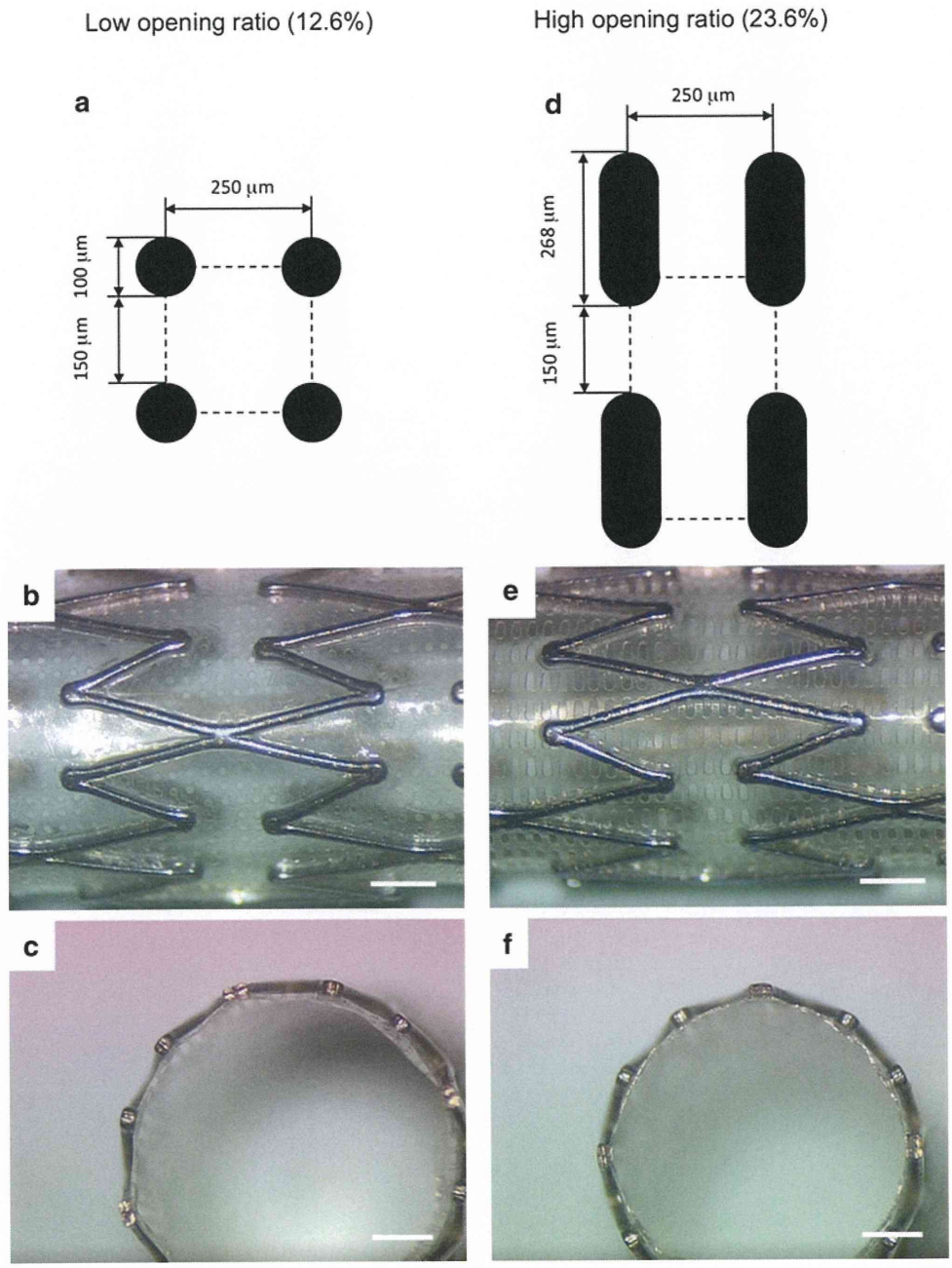

Fig. 1 Two types of stent grafts prepared using Luminexx self-expanding stents (5 × 20 mm). **a–c** Circular pore type with a low opening ratio of 12.6% (circular pore: diameter 100 μm, interpore distance 250 μm). **d–f** Bale-shaped pore type with a large opening ratio of 23.6% (bale-shaped pore: size 100 × 268 μm, interpore distance 250 μm). **a**, **d** Pore design, **b**, **e** microscopic photos showing that micropores were standardized over the film, **c**, **f** cross sections showing stent struts embedded in the polyurethane thin microporous films. *Bar* 1.0 mm

indicating the luminal surface of the stent graft was smooth and flat (Figs. 1c, f, 2h). As shown in our previous study [4], the shape of the expanded stent graft and its mechanical properties, such as the flexibility of the covering, did not change regardless of either the covering or the pore density. It is possible to shrink the stent grafts using a hand-held crimping device without any damage to the cover film. The shrinking process is shown in Fig. 2. Therefore, stenting procedures were performed using a standard endoscopic procedure without difficulty.

Aneurysm occlusion was achieved immediately at $\leq$10 min after stenting of the both stent grafts without post-dilation. Angiography at 1 month post-implantation of the stent grafts or bare stents revealed that all parent arteries were patent without significant stenosis. All aneurysms with the stent grafts were still occluded, while aneurysms with simple bare self-expanding stents were all patent (Fig. 3).

Histology

In specimens obtained 1 month post-implantation of both types of self-expanding stent grafts, the aneurysm cavity was packed with the marked proliferation of granulomatous tissue. The luminal surface of the stent graft was covered with a thin layer of fibrous tissue and endothelial cells (Fig. 4d, e). The orifice of the aneurysm was completely covered with this layer (Fig. 4b, c). In comparison, in carotid arteries with the bare control stents in place, the luminal surface of the stent was covered with similar fibrous tissues except for the neck of the aneurysm (Fig. 4a).

Intimal thickness was lower with the self-expanding stent with a high opening ratio than with its counterpart with a low opening ratio or the bare stent. (Fig. 4f). Statistically significant differences were shown by the t test between bare stents (0.341 ± 0.146 mm) and self-expanding stent grafts with a low pore density (0.441 ± 0.129 mm, $p = 0.0206 < 0.05$), between bare stents and self-expanding stent grafts with a high pore density (0.187 ± 0.098 mm, $p < 0.0001$), and between self-expanding stent grafts with low versus high pore density ($p < 0.0001$).

Discussion

We have been developing high-performance, self-expanding stent grafts for the occlusion of large or giant cerebral aneurysms that are difficult to treat by traditional surgical or endovascular methods [5]. The ease of delivery and good embolization effects of these stent grafts in experimental aneurysms in dogs at 1 month post-implantation have already been demonstrated. The stent graft consists of a self-expanding stent with a thin SPU film (dip-coating method) on which with micropores have been created with an excimer laser ablation technique, followed by coating with argatroban. Polyurethane has excellent elastomeric properties and is clinically used as a material for blood pumps and arterial grafts; it also exhibits no toxicity or little biodegradation [6–8]. In previous studies, we demonstrated its good biocompatibility in a series of experiments involving dogs and rabbits with follow-up periods ranging from 1 month up to 3 years. On the other hand, argatroban, an

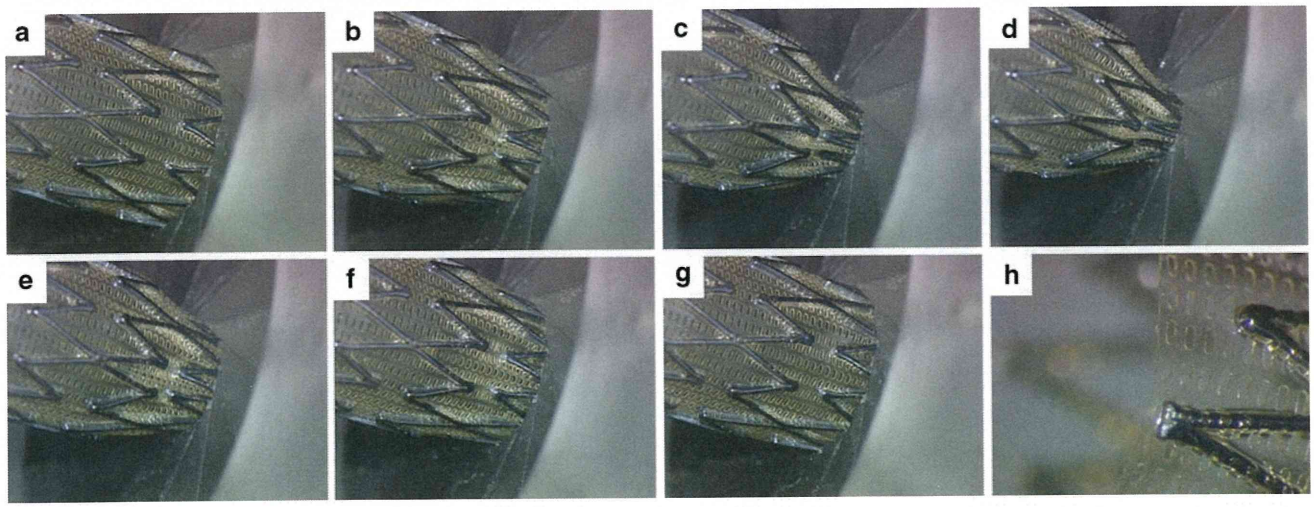

Fig. 2 Shrinking operation of the stent graft with bale-shaped pores for mounting to the delivery catheter. **a** A half of the original stent graft was inserted into the hand-crimping device. **b–d** Shrinking process, **d–g** de-shrinking process. **h** The terminal shape of the cover film after shrinking. There was no damage to the cover film after shrinking

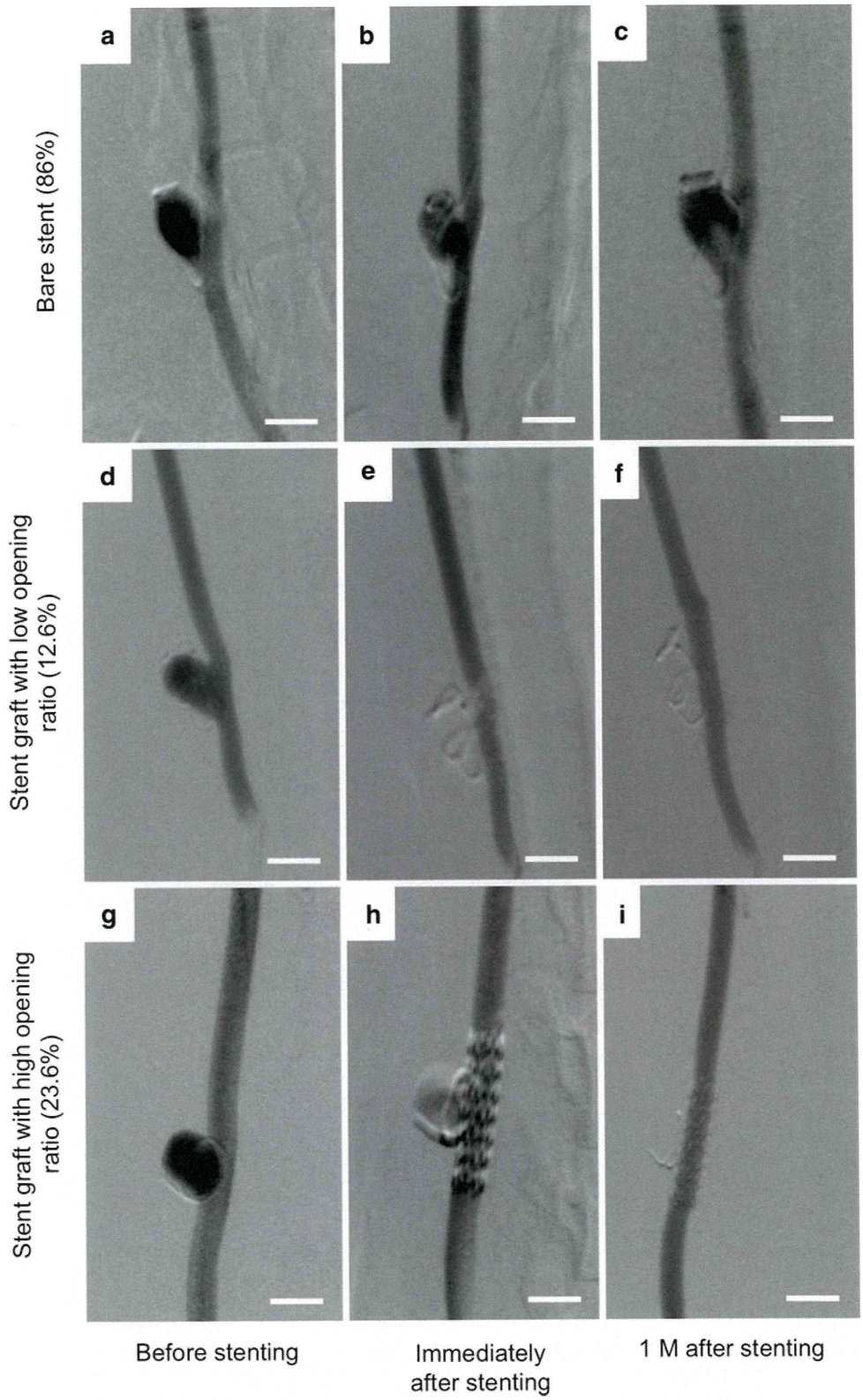

Fig. 3 Beagle carotid arteriograms showing an experimentally created lateral-wall aneurysm with a control bare stent in place (**a–c**), or with stent grafts having a low opening ratio (**d–f**) or a high opening ratio (**g–I**) in place. **a**, **d**, **g** Anterior–posterior arteriograms showing broad-based lateral-wall aneurysms of the common carotid arteries (approx. diameter of parent vessel 4.5–5 mm). **e** Immediately after transfemoral placement of a stent graft with a low opening ratio, complete obliteration of the aneurysm with patency of the parent vessel was obtained. **h** A stent graft with a high pore density showing incomplete obliteration of the aneurysm with a small residual aneurysmal space and patency of the parent vessel. **b** A control bare stent showing a completely patent aneurysm. **f**, **I** Angiogram 1 month post-placements of stent grafts demonstrating complete occlusion of the aneurysms without significant narrowing of the parent vessels. **c** A control bare stent demonstrating a patent aneurysm. *Bar* 1.0 mm

arginine-derived synthetic low-molecular-weight compound that binds to thrombin, competitively inhibits fibrinogen cleavage and the platelet activation stimulated by thrombin [9, 10]. These properties have resulted in argatroban being used for designing antithrombogenic surfaces in percutaneous transluminal angioplasty (PTA) devices, including balloon catheters and stents [11, 12].

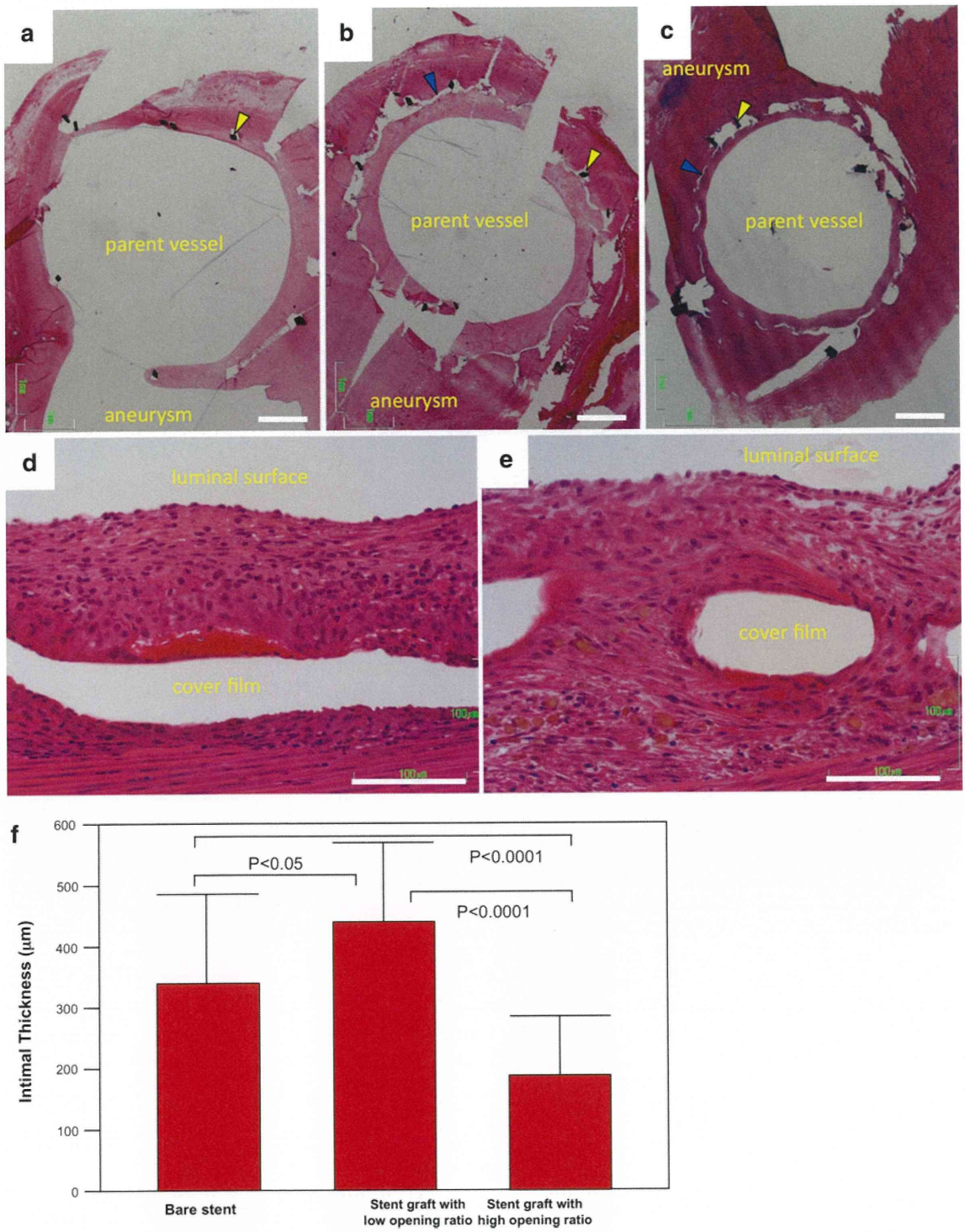

Fig. 4 Cross-sectional micrographs of aneurysms treated with a control bare stent (**a**) and self-expanding stent grafts with a low opening ratio (**b**) or a high opening ratio (**c**, **d** on the cover film, **e** around micropores), 1 month post-implantation (hematoxylin and eosin stain: *yellow arrowheads* stent strut, *blue arrowheads* cover film). Organized thrombus formation is visible within the aneurysm as is mild intimal fibro-cellular proliferation of the parent vessel wall in those with self-expanding stent grafts; in contrast, there is no aneurysmal tissue formation in the aneurysms with control bare stents in place. The neck of the aneurysm corresponds to the arterial wall defect at the side-to-end anastomotic site of the carotid artery and the venous pouch. The luminal surface of the stent graft with a high opening ratio was covered with a thin layer of fibrous tissue and endothelial cells. *Bar* (**a–c**) 1.0 mm, (**d**, **e**) 100 μm (**d**, **e**). **f** Intimal thicknesses at 1 month post-implantation of stents. Intimal thickness was lower with a high opening ratio (23.6%, 187 ± 98 μm) relative to that with a low opening ratio (12.6%, 441 ± 129 μm) or a bare stent (86%, no pores, 341 ± 146 μm). A statistically significance difference was shown by the *t* test

In our study, the self-expanding stent grafts with a high opening ratio of 23.6% showed less intimal hyperplasia than the control bare stents or self-expanding stent grafts with a low opening ratio of 12.6% at 1 month post-occlusion of canine aneurysms. All aneurysms were occluded by self-expanding stent grafts, while aneurysms were patent when treated with bare stents.

Giant, large dissecting, or wide-neck aneurysms treated with coils carry a greater risk of recurrence [13–16], namely, 87% for giant wide-necked aneurysms [17] and 50% for dissecting aneurysms [18]. The causes of this recurrence include incomplete and loose coil packing during embolization, coil compaction or migration into the intra-aneurysmal fresh thrombus, spasm relief in the aneurysm neck and/or parent vessel, thrombus organization, and fibrosis in the aneurysm cavity after embolization [19]. Coiling of giant intracranial aneurysms can on occasion exacerbate symptoms due to a mass effect [16, 20], and fatal hemorrhage has occurred after incomplete occlusion [14]. Thus, the coiling of aneurysms has a limited capacity.

In such situations as described above, the stenting of cerebral aneurysms is useful for blocking coil protrusion, as well as for the alteration of inflow characteristics leading to thrombosis and occlusion, as shown in experimentally induced sidewall and fusiform aneurysms in an animal model [21]. The woven wire mesh of the stent interferes with blood flow patterns and promotes thrombosis and fibrosis within the residual aneurysmal lumen. Variations in clinical results are reportedly due to unpredictable blood flow alterations after porous stent placement [22]. However, little information in available on stent-related problems, such as intimal hyperplasia, and such problems may seriously affect long-term results. In rats and rabbits, accelerated endothelialization may reduce neointimal formation after balloon angioplasty or stent placement [23, 24]. Our microporous membrane induces early endothelialization soon after stent graft implantation, thereby avoiding early thrombosis and controlling mid- to long-term hyperplasia [25]. Proliferative reactions have been found to be more remarkable in vessels containing balloon-expandable stents than with a self-expanding prosthesis [26], primarily due to intimal–medial injury caused by dilation of the stent toward the arterial wall [27].

The advantages of stent grafts over coils or liquid embolic materials or bare stents include reconstruction of the parent artery, immediate occlusion, decreased recurrence rates, reduced rupture without a direct approach to the aneurysmal dome, and decreased mass effects [28]. The development of biodegradable, nonparticulating material with an antithrombogenic coating has reduced the formerly high rates of subacute thrombosis and myointimal proliferation [29]. In addition to a transoral antiplatelet agent (clopidogrel), our stent grafts are coated with a thrombin-selective anticoagulant (argatroban) for the prevention of early thrombus. Stents covered with endothelial cells capable of secreting large amounts of tissue plasminogen activator may reduce the risk of thrombosis [30]. In a previous study in which we used our balloon-expandable stent grafts in a canine aneurysm embolization model, the luminal surface of the arteries was already covered with confluent endothelial cells at 1 week post-graft implantation [3].

Although more porous PTFE prostheses reportedly induce faster transprosthetic endothelialization, an increase in pore size does not necessarily improve the performance of a graft [31, 32]. In baboons, PTFE grafts with an optimal internodal distance of 60 mm were found to be completely and effectively covered with an endothelialized neointima within 1 month, in contrast to those with 30- or 90-mm internodal grafts [33, 34].

Polyurethanes have good elasticity and well-documented bio- and blood compatibility [35–37]. Polyurethane-covered stents implanted in the mini-pig aorta have shown good biocompatibility with minimal vessel wall inflammation [38]. An in vitro study showed increased endothelial cell coverage in polyurethane-covered stents as compared with bare stents [39]. The development of polyurethane with a higher permeability and pore size (normal permeability 1,200 ml/min/cm^2, pore size 40–50 μm) has led to a reduced neointimal area as compared to the low-permeability polyurethane (low permeability 280 ml/min/cm^2, pore size <20–25 μm) [32]. In an in vitro model of transmural endothelialization in open-cell-structured, small-diameter polyurethane vascular grafts, the larger the pores used, the higher the endothelialization rate. The highest endothelialization rate was found on films with micropores between 18 and 50 μm in diameter [40]. In rat, rabbit, and baboon models, there seems to be an optimal pore size for adequate neointimal endothelialization: pores that are too small decrease endothelialization and stimulate neointima formation, while pores that are too large lead to endothelial defects with the potential of thrombosis [33].

In one study on balloon-expandable stent graft implantation in beagles using SPU film with four micropore densities around the circumference (i.e., no pores, and pores with a 30-μm diameter with orderly interpore distances of 250, 500 and 125 μm, respectively), the neointimal layer was thinnest with a 125-μm interpore distance [25]. For practical fabrication of the microporous SPU film, we use a film with a 100-μm pore diameter and 250-μm interpore distance (low opening ratio 12.6%) in the balloon-expandable stent grafts. These self-expanding stent grafts, with a bale-shaped pore of size 100 × 268 μm and a 250-μm interpore distance (high opening ratio 23.6%), were put in place. On angiography 1 month later, all

carotid arteries were patent without significant stenosis regardless of the self-expanding stent type used. All aneurysms treated with these stent grafts were occluded, while those treated with control bare stents were patent. Histologically, our high-performance self-expanding stent graft with a high opening ratio (23.6%) showed less intimal hyperplasia than a bare stent or the stent graft with low opening ratio (12.6%). A pore ratio of 23.6% was thus found to control intimal growth in our study.

A new intracranial Willis balloon-expandable fully-covered stent with a 3.8 Fr outer diameter has been developed and applied to very large and giant aneurysms. This stent consists of 3 parts, a bare multi-segment stent with a thickness ranging from 30 to 50 μm and staggered connecting-points, an expandable thin polytetrafluoroethylene (ePTFE) membrane 10 mm in thickness, and a low-pressure flexible balloon catheter [28]. Recurrent aneurysms of the internal carotid artery in 7 patients and the vertebral artery in 1 patient were favorably occluded with patency of the parent artery [5, 41].

Access issues, post-stenting stenosis due to multilayer neointimal proliferation, and possible closure of the side branches by fully covered stents are issues awaiting resolution [22, 42]. To the avoid occlusion of tiny vessels, such as perforators, partially covered stent grafts [43] or our novel high-performance stent grafts are potentially useful and should be considered as alternative devices.

Conclusion

Our self-expanding stent grafts were easily applied to experimental aneurysms and achieved complete aneurysm occlusion in beagles at 1 post-implantation. The stent graft with a high opening ratio (23.6%) was associated with less intimal hyperplasia than a bare stent or a stent graft with low opening ratio (12.6%). The pore ratio of 23.6% was thus found to control intimal growth. The newly developed stent graft performed well in terms of creating less intimal hyperplasia and in the embolization effect. Further series of experiments, including a longer follow-up study, must be performed prior to clinical application.

References

1. Cragg AH, Dake MD. Treatment of peripheral vascular disease with stent-grafts. Radiology. 1997;205:307–14.
2. Palmaz JC. Review of polymeric graft materials for endovascular applications. J Vasc Interv Radiol. 1998;9:7–13.
3. Nishi S, Nakayama Y, Ishibashi-Ueda H, Matsuda T. Occlusion of experimental aneurysms with heparin-loaded, microporous stent grafts. Neurosurgery. 2003;53:1397–405.
4. Nishi S, Nakayama Y, Ishibashi-Ueda H, Okamoto Y, Kinoshita Y. High performance self-expanding stent graft; development and application to experimental aneurysms. J Artif Organs. 2009;12:35–9.
5. Li MH, Li YD, Fang C, Gu BX, Wang W, Cheng YS, Wang YL, Gao BL, Zao JG, Wang J, Li M. Endovascular treatment of giant or very large intracranial aneurysms with different modalities: analysis of 20 cases. Neuroradiology. 2007;49:819–28.
6. Xue L, Greisler HP. Biomaterials in the development and future of vascular grafts. J Vasc Surg. 2003;37:472–80.
7. Farrar DJ, Litwak P, Lawson JH, Ward RS, White KA, Robinson AJ, Rodvien R, Hill JD. In vivo evaluations of a new thrombo-resistant polyurethane for artificial heart blood pumps. J Thorac Cardiovasc Surg. 1988;95:191–200.
8. Giancario M, Mirko DO, Lacono C, Rozzanigo U, Serio G, Procacci C. Gastrointestinal artery stamp haemorrhage following pylorus-sparing whipple procedure: treatment with covered stents. Dig Surg. 2002;19:237–40.
9. Kikumoto R, Tamao Y, Tezuka T, Tonomura S, Hara H, Ninomiya K, Hijikata A, Okamoto S. Selective inhibition of thrombin by (2R, 4R)-4-methyl-1-[N2-[(3-methyl-1, 2, 3, 4-tetrahydro-8-quinolinyl) sulfonyl]-l-arginyl]]-2-piperidinecarboxylic acid. Biochemistry. 1984;23:85–90.
10. Kumada T, Abiko Y. Comparative study on heparin and a synthetic thrombin inhibitor no. 805 (MD-805*) in experimental antithrombin III-deficient animals. Thromb Res. 1981;24:285–98.
11. Imanishi T, Arita M, Hamada M, Tomobuchi Y, Hano T, Nishio I. Effects of locally administration of argatroban using a hydrogel-coated balloon catheter on intimal thickening induced by balloon injury. Jpn Circ J. 1997;61:256–62.
12. Richey T, Iwata H, Oowaki H, Uchida E, Matsuda S, Ikada Y. Surface modification of polyethylene balloon catheters for local drug delivery. Biomaterials. 2000;21:1057–65.
13. Vinuela F, Duckwiler G, Mawad M. Guglielmi detachable coil embolization of acute intracranial aneurysms: perioperative anatomical and clinical outcome in 403 patients. J Neurosurg. 1997;86:475–82.
14. Ross IB, Weil A, Piotin M, Moret J. Endovascular treatment of distally located giant aneurysms. Neurosurgery. 2002;47:1147–52.
15. Mordasini P, Schroth G, Guzman R, Barth A, Seiler RW, Remonda L. Endovascular treatment of posterior circulation cerebral aneurysms by using Guglielmi detachable coils: a 10-year single center experience with special regard do technical development. AJNR Am J Neuroradiol. 2005;26:1732–8.
16. Fiorella D, Albuquerque FC, McDougall CG. Durability of aneurysm embolization with matrix detachable coils. Neurosurgery. 2006;58:51–9.
17. Magoufis GL, Vrachliotis TG, Stringaris KA. Covered stents to treat partial recanalization of Onyx-occluded giant carotid aneurysm. J Endovasc Ther. 2004;11:742–6.
18. Ahn JY, Han IB, Kim TG, Yoon PH, Lee YJ, Lee BH, Seo SH, Kim DI, Hong CK, Joo JY. Endovascular treatment of intracranial vertebral artery dissection with stent placement or stent-assisted coiling. AJNR Am J Neuroradiol. 2006;27:1514–20.
19. Gallas S, Pasco A, Cottier JP, Gabrillargues J, Drouineau J, Cognard C, Herbreteau D. A multicenter study of 705 ruptured intracranial aneurysms treated with Gugliemi detachable coils. AJNR Am J Neuroradiol. 2005;26:1723–31.
20. Malisch TW, Guglielmi G, Vinuela F, Duckwiller G, Goin YP, Martin N, Frazee J. Intracranial aneurysms treated with Guglielmi detachable coils: midterm clinical results in a consecutive series of 100 patients. J Neurosurgery. 1997;28:219–39.
21. Geremia G, Brack T, Brennecke L, Haklin M, Falter R. Occlusion of experimentally created fusiform aneurysms with porous metallic stents. AJNR Am J Neuroradiol. 2000;21:739–45.

22. Krings T, Busch B, Sellhaus B, Drexler AY, Bovi M, Hermanns-Sachweh B, Scherer K, Gilsbach JM, Thron A, Hans FJ. Long-term histological and scanning electron microscopy results of endovascular and operative treatments of experimentally induced aneurysms in the rabbit. Neurosurgery. 2006;59:911–24.
23. Asahara T, Bauters C, Pastore CJ, Keamey M, Rossow S, Bunting S, Ferrara N, Symes JF, Isner JM. Local delivery of vascular endothelial growth factor accelerates re-endothelialization and attenuates intimal hyperplasia in balloon-injured rat carotid artery. Circulation. 1995;91:2793–801.
24. Van Belle E, Maillard L, Tio FO, Isner JM. Accelerated endothelialization by local delivery of recombinant human endothelial growth factor reduces in-stent intimal formation. Biochem Biophys Res Commun. 1997;235:311–6.
25. Nishi S, Nakayama Y, Ueda H, Ishikawa M, Matsuda T. A new stent graft with thin walled controlled micropored polymer covering. Intervent Neuroradiol. 2000;6[Suppl 1]:175–80.
26. Chuapetcharasopon C, Wright KC, Wallace S, Dobben RL, Gianturco C. Treatment of experimentally induced atherosclerosis in swine iliac arteries; a comparison of self-expanding and balloon-expanded stents. Cardiovasc Intervent Radiol. 1992;15:143–50.
27. Waller BF, Orr CM, Pinkerton CA, Van Tassel JW, Pinto RP. Morphologic observation late after coronary balloon angioplasty: mechanisms of acute injury and relationship to restenosis. Radiology. 1990;174:961–7.
28. Li MH, Zhu YO, Fang C, Wang W, Zhang PL, Cheng YS, Tan HO, Wang JB. The feasibility and efficacy of treatment with a Willis covered stent in recurrent intracranial aneurysms after coiling. AJNR Am J Neuroradiol. 2008;29:1395–400.
29. Serruys PW, Strauss BH, Beatt KJ, Bertrand ME, Puel J, Rickards AF, Meier B, Goy JJ, Vogt P, Kappenberger L. Angiographic follow-up after placement of a self-expanding coronary artery stent. N Engl J Med. 1991;324:13–7.
30. Flugelman MY, Virmani R, Leon MB, Bowman RL, Dichek DA. Genetically engineered endothelial cells remain adherent and viable after stent deployment and exposure to flow in vitro. Circ Res. 1992;70:348–54.
31. Kusaba A, Fischer CR, Matulewskin TJ, Matsumoto T. Experimental study of the influence of porosity on development of neointima in Goa Tex grafts: a method to increase long-term patency rate. Am Surg. 1981;47:347–54.
32. Schürmann K, Haage P, Meyer J, Vorwerk D, Klosterhalfen B, Großkortenhaus S, Hartmann J, Kulisch A, Günther RW. Comparison of two stent-grafts with different porosity: in vivo studies in a sheep model. J Vasc Interv Radiol. 2000;11:493–502.
33. Golden MA, Hanson SR, Kirkman TR, Schneider PA, Clowes AW. Healing of polytetrafluoroethylene arterial grafts is influenced by graft porosity. J Vasc Surg. 1990;11:838–45.
34. Clowes AW, Zacharias RK, Kirkman TR. Early endothelial coverage of synthetic arterial grafts: porosity revisited. Am J Surg. 1987;1553:501–4.
35. Boretos JW, Pierce WS. Segmented polyurethane: a new elastomer for biomedical applications. Science. 1967;158:1481–2.
36. Grasel TG, Cooper SL. Surface properties and blood compatibility of polyurethaneureas. Biomaterials. 1986;7:315–28.
37. Szycher M, Siciliano AA, Reed AM. Polyurethanes in medical devices. Med Des Mater. 1991;1:18–25.
38. Horita N, Tomita H, Takamuro M, Fuse S, Tsutsumi H. Development of a reexpandable covered stent for children. Catheter Cardiovasc Interv. 2006;68:727–34. (discussion p. 735)
39. Müller-Hülsbeck S, Wallusche ck KP, Priebe M, Grimm J, Cremer J, Heller M. Experience on endothelial cell adhesion on vascular stents and stent-grafts: first in vitro results. Invest Radiol. 2002;37:314–20.
40. Matsuda T, Nakayama Y. Surface microarchitectural design in biomedical applications; in vitro transmural endothelialization on microporous segmented polyurethane films fabricated using an excimer laser. J Biomed Mater Res. 1996;31:235–42.
41. Li MH, Gao BL, Wang YL, Fang C, Li YD. Management of pseudoaneurysms in the intracranial segment of the internal carotid artery with covered stents specially designed for use in the intracranial vasculature: technical notes. Neuroradiology. 2006;48:841–6.
42. Krings T, Hans FJ, Möller-Hartmann W, Brunn A, Thiex R, Schmitz-Rode T, Verken P, Scherer K, Dreeskamp H, Stein KP, Gilsbach JM, Thron A. Treatment of experimentally induced aneurysms with stents. Neurosurgery. 2005;56:1347–60.
43. Zhong H, Matsui O, Xu K, Ogi T, Okuda M, Liu Y, Sanada J, Sun C. Partially covered stent-graft implantation in rabbit aorta: a new model to investigate bioactive stent-grafts in small animals. J Endovasc Ther. 2009;16:154–60.

J Artif Organs (2011) 14:276–283
DOI 10.1007/s10047-011-0596-2

ORIGINAL ARTICLE

Variations in local elastic modulus along the length of the aorta as observed by use of a scanning haptic microscope (SHM)

Takeshi Moriwaki · Tomonori Oie · Keiichi Takamizawa · Yoshinobu Murayama · Toru Fukuda · Sadao Omata · Keiichi Kanda · Yasuhide Nakayama

Received: 2 February 2011 / Accepted: 13 July 2011 / Published online: 20 August 2011

Abstract Variations in microscopic elastic structures along the entire length of canine aorta were evaluated by use of a scanning haptic microscope (SHM). The total aorta from the aortic arch to the abdominal aorta was divided into 6 approximately equal segments. After embedding the aorta in agar, it was cut into horizontal circumferential segments to obtain disk-like agar portions containing ring-like samples of aorta with flat surfaces (thickness, approximately 1 mm). The elastic modulus and topography of the samples under no-load conditions were simultaneously measured along the entire thickness of the wall by SHM by using a probe with a diameter of 5 μm and a spatial resolution of 2 μm at a rate of 0.3 s/point. The elastic modulus of the wall was the highest on the side of the luminal surface and decreased gradually toward the adventitial side. This tendency was similar to that of the change in the elastin fiber content. During the evaluation of the mid-portion of each tunica media segment, the highest elastic modulus (40.8 ± 3.5 kPa) was identified at the thoracic section of the aorta that had the highest density of elastic fibers. Under no-load conditions, portions of the aorta with high elastin density have a high elastic modulus.

Keywords Microscope · Elastic modulus · Aorta · Micromechanics · Extracellular matrix

T. Moriwaki · T. Oie · K. Takamizawa · Y. Nakayama (✉)
Division of Medical Engineering and Materials, National Cerebral and Cardiovascular Center Research Institute, 5-7-1 Fujishiro-dai, Suita, Osaka 565-8565, Japan
e-mail: nakayama@ri.ncvc.go.jp

T. Moriwaki · Y. Nakayama
Cell Engineering Unit, Graduate School of Chemical Science and Engineering, Hokkaido University, Sapporo, Japan

T. Oie (✉)
Shinkan Kogyo Co., 3-4-15 Takeshima, Yodogawa-ku, Osaka 555-0011, Japan
e-mail: oie@polka.plala.or.jp

Y. Murayama · T. Fukuda · S. Omata
College of Engineering, Nihon University, Fukushima, Japan

K. Kanda
Department of Cardiovascular Surgery, Kyoto Prefectural University of Medicine, Kyoto, Japan

Introduction

The mechanical properties of the aorta, the main component of the blood circulatory system originating from the heart, vary in diseases such as hypertension or atherosclerosis. The arterial media wall consists of 2 main extracellular matrices of elastin fibers or collagen fibrils, which are highly flexible and pressure-resistant in mechanical properties. Elastic modulus, one of the general indices of mechanical properties, is typically measured as macroscopic strain induced by the application of force in a tensile test. In previous studies, differences between the elastic modulus of different segments of the aorta [1–5], differences during the aging process [6], and its physiology and pathology [7, 8], have been reported on the basis of results of tensile tests. Tensile tests are quite simple and suitable for macroscopic mechanical evaluations, but are not appropriate for determination of local elastic modulus inside the aortic tissue. In addition, the test cannot be used for replicate or continuous measurements because it involves sample destruction.

On the other hand, atomic force microscopy (AFM) has been used to make measurements of local elastic modulus

within the microscopic area [9]. AFM enables resolution at the nanometer scale because it uses sharp pyramidal tips with a radius range of 20–60 nm. However, because the scanning area in AFM is usually less than 10 μm, measurements in the sub-millimeter range, which are appropriate for vascular tissue samples, are extremely difficult to obtain. Therefore, some components of vascular tissue, for example collagen fibrils, are difficult to measure [10, 11]. Recently, a simple and inexpensive microindentation system, which uses large indenter tips with a radius of approximately 170 μm, was developed for measurement of the spatial organization of the microscale elastic properties of fully hydrated soft gels or tissues [12]. Additionally, Matsumoto et al. [13] measured mechanical properties of the lamellar unit of porcine aorta by use of scaled-up AFM.

In our previous study, a scanning haptic microscope (SHM) system was developed to enable convenient observation of the distribution of the elastic modulus over slices of natural tissue samples [14–16]. This system is based on tactile sensor technology [14], which can measure the elastic modulus of living tissue at cellular [15] and organ [16] levels. SHM has recently been applied in measurements of the distribution of elastic modulus in a blood vessel in which elastic construction across the entire circumferential cross-section of the aortic wall was observed in saline solution without invasion of the isolated specimen [17]. This technique was also used to reveal that the elastin-rich and collagen-rich areas are clearly segregated in terms of elastic modulus [18]. Therefore, SHM is a powerful tool for evaluating the local elastic modulus of living tissues with micrometer precision.

In this study, segmental elastic analysis was microscopically performed along the entire length of a canine aorta. Previous traditional macroscopic studies have indicated that the strength of the aorta differs across sections because the tissue includes components with different densities, for example elastin or collagen, and cells of different density, for example smooth muscle cells (SMC). These components seem to differ across different sections [8, 19]. This SHM study reveals differences in local elastic modulus of the extracellular matrix of different segments.

Materials and methods

Preparation of aortic tissue samples

The animals used in this study received care in accordance with the Principles of Laboratory Animal Care (formulated by the National Institutes of Health, Publication No. 56-23, received 1985), and the research protocol (No. 10064) was approved by the ethics committee of the National Cardiovascular Center Research Institute.

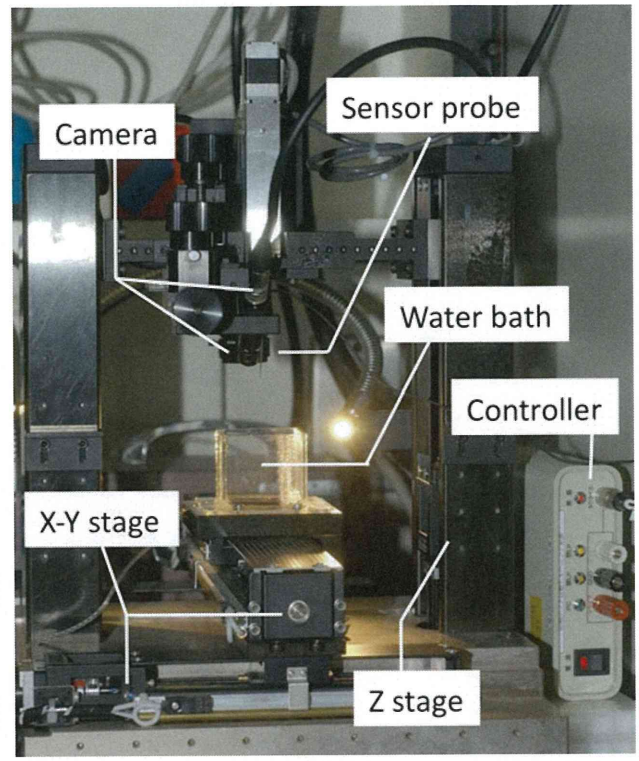

Fig. 1 Photograph of a scanning haptic microscope (SHM) system, which includes 5 different components: a water bath including sample holder, 2 different stages for *X–Y-* and *Z*-axis movements, a sensor probe, 2 cameras, and a controller

Canine aortas were harvested from beagles (age, ca. 300 days; body weight, ca. 7 kg). The entire length of an aorta was cut into 6 approximately equal segments. Each segment was in the form of a tube with a length of ca. 5 cm (Fig. 2). Photographs were taken with a scale to measure the internal diameter of each segment.

Scanning haptic microscope overview

The local elastic modulus images of aortic cross-section samples were measured by SHM. Specific descriptions of the device configuration and measurement principles have been given elsewhere [14–18]. Briefly, the SHM system is composed of 5 units: a water bath, stages, a microtactile sensor, cameras, and a controller (Fig. 1). The water bath (custom-designed in our laboratory) is mounted along the *XY*-axis stage (P&M, Fukushima, Japan) for horizontal movement to make measurements in a liquid environment. The microtactile sensor is fixed on the Z-axis stage (P&M) for vertical movement. The 2 stages employ 0.01 mm resolution stepping motors, and are controlled by a personal computer with customized software. Two cameras are installed in the system. One camera (WAT-231S2; Watec, Tsuruoka, Japan) is installed behind the sensor probe to enable observation of the entire sample area and

the setting of the measurement area. The other camera (CS9401-03; Toshiba Teli, Tokyo, Japan) is installed in front of the sensor probe to enable observation of the contact between the sensor tip and the sample surface.

The sensor probe includes a glass needle and a lead zirconate titanate (PZT) sensor element. There are 3 electrodes in the PZT sensor element, input, output, and ground. Operation of the sensor unit is based on the phase-shift method [20]. The sensor probe is vibrated near the resonance frequency by applying an AC voltage to the PZT sensor element, and the vibration state is maintained, by means of a phase-shift circuit present in the controller, as a feedback circuit for the vibration phase. A frequency change is generated by contact between the sensor tip and the sample surface and this frequency change has an almost linear relationship with the elastic modulus of the sample. Therefore, mapping a pattern of frequency change at each point across the entire measurement area indicates the microstructure of the elastic modulus of a sample.

SHM measurement

In the work discussed in this paper, surface elastic modulus was measured in horizontal sections relative to the circumferential direction of the canine aorta. A part of each aorta was embedded in 4% agar (Nacalai Tesque, Kyoto, Japan) in the no-load state, and cut into horizontally circumferential slices 1 mm thick by use of a microtome (VT1200S; Leica Microsystems Japan, Tokyo, Japan) to obtain disk-like portions containing ring-like samples of aorta with flat surfaces.

The SHM measurement was performed in accordance with our previous report [17, 18]. Briefly, the samples ($n = 3$ per each segment) were fixed with a sample holder on the bottom of the water bath. A movie camera was used to monitor the surface of the sample and the tip of the sensor probe, which was calibrated using the force–deformation method with a 1-mm diameter metal rod indenter and agar gel (concentrations 1–3 wt%, elastic modulus 9–95 kPa). The bath was filled with a saline solution at a specified depth, which was selected for acquisition of the maximum change in frequency and the minimum frequency fluctuation of the sensor on the agar gel. The SHM measurement was carried out without any preconditioning according to the previously reported method in a point-by-point manner. The distance between 2 adjacent scanned points was 2 μm. The tip radius and indentation depth of the sensor probe were 5 and 10 μm, respectively. The overall scanning speed was approximately 3 points/s. The scanning area of each image was 200 × 200 μm (number of pixels, 10,000 points). The scanning measurements were repeated for the entire wall of the aorta. In the elastic images obtained by this method, stiff regions were defined as being stiffer than 1.15× the average elastic modulus. Such stiff regions are expected to be mainly composed of elastin. Soft regions were defined as being softer than 0.85× the average elastic modulus. Such soft regions are expected to be mainly composed of collagen and SMCs.

Histological examination

After the SHM measurements, disk-like samples 1 mm thick after SHM measurements were cut using a microtome and fixed with 10% formalin, embedded in paraffin, sliced into circumferential 4-μm-thick sections, and stained with Elastica-van Gieson stain for elastin or Masson's trichrome stain for collagen. The stained images were analyzed by use of Photoshop software (Adobe Systems, San Jose, CA, USA). The wall thickness of the samples was determined for the stained images.

Results

To obtain samples, the entire canine aorta was equally divided into 6 segments as indicated in Fig. 2. The internal diameter of the proximal side of the aortic arch was approximately 8 mm and gradually decreased in diameter toward the distal side of the abdominal aorta (approximately 5 mm). The wall thickness of the aorta steadily decreased from the arch (approximately 1.2 mm) to the abdominal aorta (approximately 0.5 mm) according to the distance from the heart.

SHM measurements, for imaging of the elastic modulus and topography in saline solution at room temperature, and optical microscopic observations after elastin or collagen staining were performed for all segments. As demonstrated in the thoracic aorta (the third segment in Fig. 2), the distribution of the elastic modulus (Fig. 3a) and topography (Fig. 3b) were simultaneously obtained for almost the entire circumferential cross-section of the aortic wall from the luminal side, including the lamina elastica interna, to the outer side. Neither surface image changed within the total measurement time (approximately 10 h). Almost all of the laminated structures of stiff and soft regions were observed on the moderately flat surface with fine wave-lined structure. In the photographs of elastin-stained (Fig. 3c) and collagen-stained (Fig. 3d) aorta, it can be seen that the stiff region consists of elastin fibers, as demonstrated in our previous work [16]. The soft region consists of a mixture of collagen fibrils and SMCs, neither of which can be segregated clearly as a difference in the elastic modulus by SHM. The elastic modulus was higher at the surface of the luminal side (56.0 ± 2.8 kPa) and decreased gradually toward the adventitial side (approximately 35–45 kPa) (Fig. 3e). This tendency was similar to

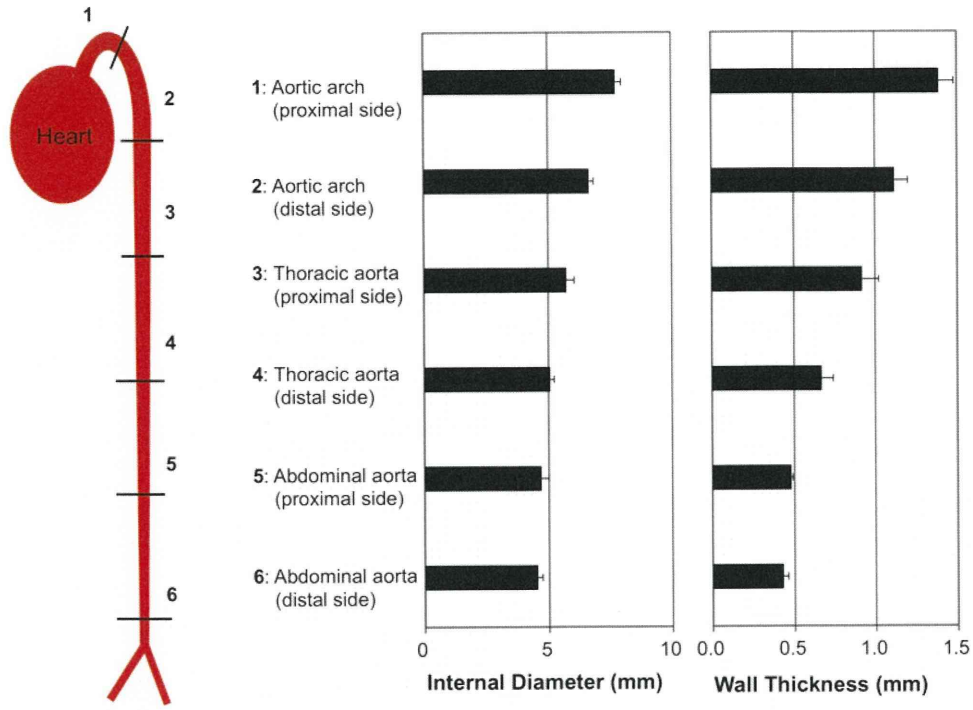

Fig. 2 Schematic representation and morphometry of samples of canine aorta under no-load conditions. The aorta was divided into 6 segments with lengths of ca. 5 cm

that of the change of elastin fiber density, where condensed elastic fibers were observed at the surface of the luminal side.

The elastic images of the segments of the aorta were compared. The series of surface elastic images at the mid portions, defined as a 200-μm width area in the central portion of the tunica media wall of each segment are summarized in Fig. 4a and in the corresponding elastin-stained photographs (Fig. 4c). The number of lines with high elastic modulus was found to increase with increasing distance from the heart to the aortic arch and then to the thoracic section. The wavy lines with high elastic modulus were observed to decrease toward the abdominal section where low and diffuse elastic images were obtained. Therefore, the total averaged elastic modulus was found to be highest on the proximal side of the thoracic aorta (40.8 ± 3.5 kPa) and lowest at both the terminal ends (proximal side of the aortic arch, 30.6 ± 3.7 kPa; distal side of the abdominal aorta, 30.6 ± 2.4 kPa) (Fig. 4b). On the other hand, the region with stained elastin fibers was observed to increase from the aortic arch (8.7%) toward the thoracic aorta (14.6%), and then to decrease toward the abdominal aorta (5.4%) (Fig. 4d). This tendency is similar to that of the change in the elastic modulus in the stiff regions of each segment, whereas the elastic modulus in the soft region tends to increase gradually with increasing distance from the heart (Fig. 4b). Therefore, under no-load conditions, the average elastic modulus value should be related to the elastic fiber content.

Discussion

The SHM measurement is noninvasive for the isolated specimen because the indentation depth of the sensor probe relative to sample surfaces is extremely low (10 μm). Therefore, it has the advantage of enabling measurements to be repeated [16]. In this study, an analysis of the elastic modulus of aorta segments under no-load conditions was performed by microscopic imaging of the local elastic structure using SHM. Because the aortic tissues were shrunken under the measurement conditions, their dimensions and mechanical properties do not correspond to the physiological state. However, it is considered meaningful that SHM imaging can clarify the variations in the local structure of tissues in different regions of a blood vessel. This is the first time SHM has been used to characterize the elastic modulus of a blood vessel. To delve deeper in this subject in the near future, we hope to perform SHM measurements on natural tissues under physiological conditions in order to characterize structural and mechanical properties.

In this study, we measured almost the entire circumferential cross-section of the aortic wall. The elastic modulus in the wall was the highest at the luminal surface side and decreased gradually toward the adventitia side. Ohashi et al. [21] reported a similar result in an investigation of the bovine thoracic aorta. The proximal side of the thoracic aorta has the highest elastic modulus in a region between the arch and the abdominal section. Interestingly, this is

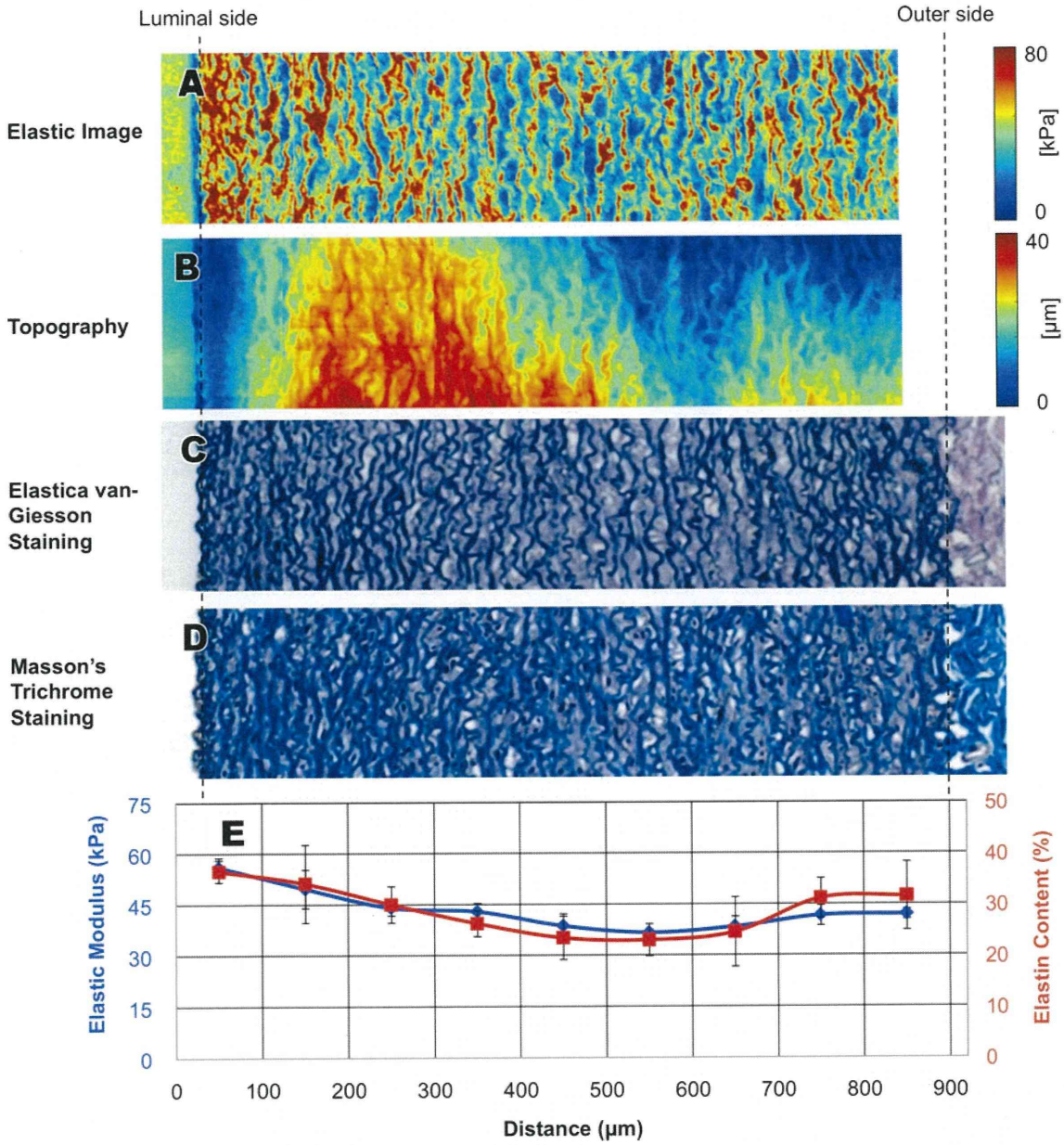

Fig. 3 Elastic image (**a**) and topography (**b**) of the thoracic aorta (the third segment in Fig. 1) obtained by SHM measurements (920 × 200 μm, 2-μm intervals). The color spectrum indicates elastic modulus (*red*, hard) in the elastic image and height (*red*, high) in topography. Elastica-van Gieson (**c**) and Masson's trichrome (**d**) staining was performed after the SHM measurements were made. The images show circumferential cross-sections of the entire thickness of the thoracic aortic wall from the intima (*left*) to the adventitia (*right*). The chart **e** shows the average elastic modulus (calculated from **a**) and elastin content (calculated from **c**) for each of the 100 × 200-μm regions

similar to the results obtained from macroscopic studies performed by Kassab [1, 2] and Sokolis [3, 4, 8]. It was considered that the tendency for mechanical properties to change with increasing distance from the heart under no-load conditions reflects the change that would be observed under physiological conditions to some extent. In traditional tensile studies it was demonstrated that aortic stiffness is related to the elastin content of the low-hemodynamic-pressure region and to the collagen content of the high-pressure region [3]. This reflects a bilateral property known as the "J" curve where both components contribute to elasticity under physiological pressure. Therefore, it was concluded that the biomechanical properties of each segment of the aorta are determined by the elastin fiber and collagen fibril content [3, 4, 8]. Our study suggests that under no-load conditions, the average elastic modulus value is related strongly to the content of the elastic fiber observed in image analysis of histological

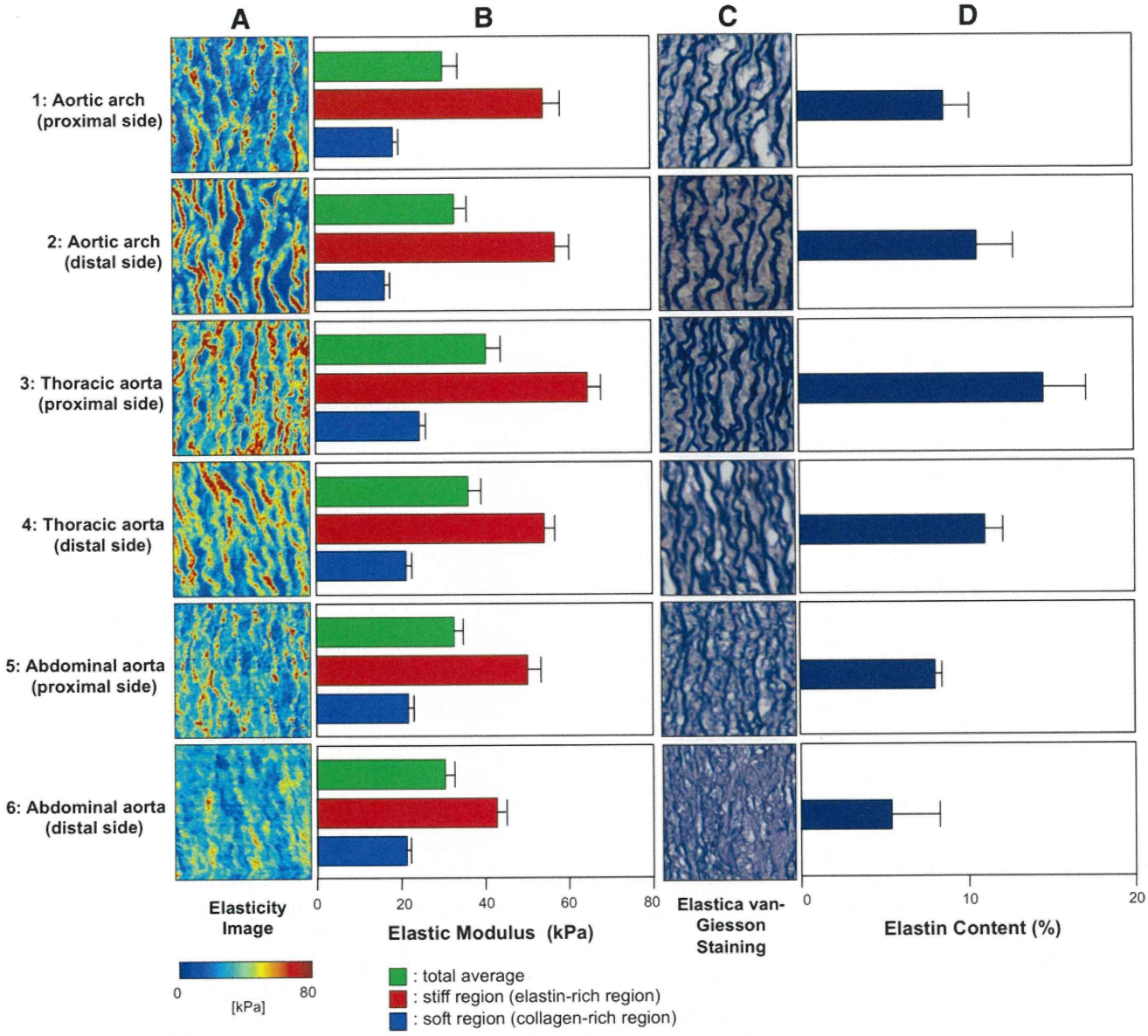

Fig. 4 Elastic images **a** of the aortic segments obtained from SHM measurements (200 × 200 μm, 2-μm intervals). The average elastic modulus **b** was calculated for the total area (*green bar*), for the stiff region (which mainly includes elastin; *red bar*), and for the soft region (which mainly comprises collagen and SMCs; *blue bar*). Stiff regions were defined as being stiffer than 1.15× the average elastic modulus. Soft regions were defined as being softer than 0.85× the average elastic modulus. Histological optical micrographs were obtained after staining with Elastica van Gieson **c** at identical magnification, and the elastin content **d** was calculated from the stained area

photographs. The aortic arch and the thoracic aorta are formed from elastic tissues types with an elastin-rich extracellular matrix. In contrast, the abdominal aorta more closely resembles collagen-rich muscle tissues. Under no-load conditions, the average elastic modulus of the aorta at different longitudinal sections increases as the elastic fiber content increases.

On the other hand, little effect of collagen content on the elastic modulus was found under these measurement conditions. This finding is in agreement with the findings of our previous report [18], which indicates that the low elastic modulus of the collagen-rich region is a result of the low density of collagen fibrils in the fully hydrated state, even though collagen fibrils have an intrinsically higher elastic modulus than elastin fibers. Gosline et al. [22] determined that elastin is 100 times less stiff than collagen. However, it was reported that collagen fibrils are in a lax state in blood vessels and do not affect the strength of the aorta under conditions of low stress [1–5, 8]. Matsumoto et al. [13] reported that the high elastic modulus region of the porcine thoracic aorta is mainly composed of elastin and that the low elastic modulus region mostly comprises SMCs. The

pattern of the elastic structure in the lamellar unit of the porcine thoracic aorta was close to the pattern observed in this study. It is unfortunate that SHM could not differentiate between the collagen fibrils and SMCs. It was considered that the contribution of the elastic modulus of these components under no-load static conditions was much lower than that of the stiff region, which mainly comprises elastin.

In this study, we compared the elastic modulus of different segments of the canine aorta. Many different conditions have an effect on elastic structure, for example age, breed, physiology, and pathology. It is very instructive to reveal these differences micromechanically. Arteriosclerosis changes not only the morphology but also the elastic modulus of elastic components. Therefore, the SHM technique may be attractive for characterizing the effects of arteriosclerosis. Furthermore, in a separate study, we have developed in vivo tissue-engineered autologous tubular tissue known as biotubes [23] and trileaflet tissues that function as biovalves [24] for use in practical regenerative medicine. SHM is expected to be a powerful tool for evaluating maturation and degree of reconstruction in treatments involving artificial tissues. This study will help to provide a precise blueprint for development of artificial tissues.

Conclusion

In this study, different elasticity under no-load condition were revealed by visualization of local elastic structure at the extracellular matrix level in different segments of the canine aorta. The thoracic proximal aorta was found to have the highest elastic modulus and the distal segments were found to have the lowest elastic modulus, according to macroscopic tensile strength measurements. We conclude that elastic modulus is related to elastin fiber content, but collagen and SMCs do not contribute significantly to the mechanical properties.

Acknowledgments The authors thank Ms Manami Sone for her technical support in this study. This study was funded in part by a Grant-in-Aid for Scientific Research (B21360123, B22390269, B23360374) from the Ministry of Education, Culture, Sports, Science and Technology of Japan.

References

1. Kassab GS. Biomechanics of the cardiovascular system: the aorta as an illustratory example. J R Soc Interface. 2006;3:719–40.
2. Guo X, Kassab GS. Variation of mechanical properties along the length of the aorta in C57bl/6 mice. AJP Heart Circ Phys. 2003;285:H2614–22.
3. Sokolis DP, Boudoulas H, Karayannacos PE. Segmental differences of aortic function and composition: clinical implications. Hellenic J Cardiol. 2008;49:145–54.
4. Sokolis DP. Passive mechanical properties and structure of the aorta: segmental analysis. Acta Physiol. 2007;190:277–89.
5. Hayashi K, Washizu T, Tsushima N, Kiraly RJ, Nose Y. Mechanical properties of aortas and pulmonary arteries of calves implanted with cardiac prostheses. J Biomech. 1981;14:173–82.
6. Osborne-Pellegrin M, Labat C, Mercier N, Challande P, Lacolley P. Changes in aortic stiffness related to elastic fiber network anomalies in the Brown Norway rat during maturation and aging. AJP Heart Circ Phys. 2010;299:H144–52.
7. Choudhury N, Bouchot O, Rouleau L, Tremblay D, Cartier R, Butany J, Mongrain R, Leask RL. Local mechanical and structural properties of healthy and diseased human ascending aorta tissue. Cardiovasc Pathol. 2009;18:83–91.
8. Angouras DC, Dosios TJ, Dimitriou CA, Chamogeorgakis TP, Rokkas CK, Manos TA, Sokolis DP. Surgical thoracic sympathectomy induces structural and biomechanical remodeling of the thoracic aorta in a porcine model. J Surg Res (in press).
9. Binnig G, Quate CF, Gerber C. Atomic force microscope. Phys Rev Lett. 1986;56:930–3.
10. Baselt DR, Revel J-P, Baldeschwieler JD. Subfibrillar structure of type I collagen observed by atomic force microscopy. Biophys J. 1993;65:2644–55.
11. Yang L, van der Werf KO, Koopman BF, Subraniam V, Bennink ML, Dijkstra PJ, Feijen J. Micromechanical bending of single collagen fibrils using atomic force microscopy. J Biomed Mater Res A. 2007;82:160–8.
12. Jacot J, Dianis S, Schnall J, Wong J. A simple microindentation technique for mapping the microscale compliance of soft hydrated materials and tissues. J Biomed Mater Res. 2006;79A: 485–94.
13. Matsumoto T, Goto T, Fukukawa T, Sato M. Residual stress and strain in the lamellar unit of the porcine aorta: experiment and analysis. J Biomech. 2004;37:807–15.
14. Murayama Y, Omata S. Fabrication of micro tactile sensor for the measurement of micro-scale local elasticity. Sens Actuators A. 2004;109:202–7.
15. Murayama Y, Constantinou CE, Omata S. Micro-mechanical sensing platform for the characterization of the elastic properties of the ovum via uniaxial measurement. J Biomech. 2004;37: 67–72.
16. Murayama Y, Constantinou CE, Omata S. Development of Tactile Mapping system for the stiffness characterization of tissue slice using novel tactile sensing technology. Sens Actuators A. 2005;120:543–9.
17. Oie T, Suzuki H, Murayama Y, Fukuda T, Omata S, Kanda K, Takamizawa K, Nakayama Y. Surface elasticity imaging of vascular tissues in a liquid environment by a scanning haptic microscope. J Artif Organs. 2010;13:121–5.
18. Oie T, Murayama Y, Fukuda T, Nagai C, Omata S, Kanda K, Yaku H, Nakayama Y. Local elasticity imaging of vascular tissues using a tactile mapping system. J Artif Organs. 2009;12: 40–6.
19. Fischer GM, Llaurado JG. Collagen and elastin content in canine arteries selected from functionally different vascular beds. Circ Res. 1966;19:394–9.
20. Omata S, Terunuma Y. New tactile sensor like human hand and its application. Sensor Actuat A. 1992;3:9–15.
21. Ohashi T, Kato Y, Matsumoto T, Sao M. Intramural distribution of elastic moduli in thoracic aortas and its relation to histology: comparison between porcine and bovine thoracic aortas, JSME International Journal. Series C. 1999;42:568–73.
22. Gosline J, Lillie M, Carrington E, Guerette P, Ortlepp C, Savage K. Elastic proteins: biological roles and mechanical properties. Phil Trans R Soc Lond B. 2002;357:121–32.
23. Watanabe T, Kanda K, Ishibashi-Ueda H, Yaku H, Nakayama Y. Autologous small-caliber "biotube" vascular grafts with

argatroban loading: a histomorphological examination after implantation to rabbits. J Biomed Mater Res B. 2010;92B: 236–42.
24. Yamanami M, Yahata Y, Uechi M, Fujiwara M, Ishibashi-Ueda H, Kanda K, Watanabe T, Tajikawa T, Ohba K, Yaku H, Nakayama Y. Development of a completely autologous valved conduit with the sinus of valsalva using in-body tissue architecture technology; a pilot study in pulmonary valve replacement in a beagle model. Circulation. 2010;122:S100–6.

Long-term animal implantation study of biotube-autologous small-caliber vascular graft fabricated by in-body tissue architecture

Taiji Watanabe,[1,2] Keiichi Kanda,[2] Masashi Yamanami,[1,2] Hatsue Ishibashi-Ueda,[3] Hitoshi Yaku,[2] Yasuhide Nakayama[1]

[1]Division of Medical Engineering and Materials, National Cerebral and Cardiovascular Center Research Institute, Suita, Osaka 565-8565, Japan
[2]Department of Cardiovascular Surgery, Kyoto Prefectural University of Medicine, Kamigyo-ku, Kyoto 602-8566, Japan
[3]Department of Pathology, National Cerebral and Cardiovascular Center, Osaka, Japan

Received 23 June 2010; revised 21 October 2010; accepted 27 January 2011
Published online 11 May 2011 in Wiley Online Library (wileyonlinelibrary.com). DOI: 10.1002/jbm.b.31841

Abstract: A mold for the preparation of an in-body tissue architecture-induced autologous vascular graft, termed "biotube," was prepared by covering a main silicone rod (outer diameter, 3 mm; length, 30 mm) with two pieces of polyurethane sponge tubes (internal diameter, 3 mm; length, 3 mm) at both ends. The molds were embedded into the dorsal subcutaneous pouch of rabbits (weighing ca. 2 kg) for 2 months. After harvesting the rods with the formed surrounding tissues, the rods were removed to create biotubes impregnated with anastomotic reinforcement cuffs at both ends. The biotubes had homogeneous, thin connective tissue wall (thickness, 76 ± 37 μm) that was primarily composed of collagen and fibroblasts. One biotube was loaded with argatroban and autoimplanted in the carotid artery for 26 months. Neither antiplatelet nor anticoagulant agents were administered, except for an intraoperative heparin injection. Follow-up angiography showed no aneurysm formation, rupturing, or stenosis during implantation. At the end of implantation, the wall thickness of biotube (212 ± 24 μm at the anastomosis portion and 150 ± 14 μm at the midportion) was similar to that of native artery (189 ± 23 μm). The luminal surface was completely covered with endothelial cells on the formed lamina elastica interna-like layer. The regenerated vascular walls comprised multilayered smooth muscle cells and dense collagen fibers with regular circumferential orientation. A remarkable multilayered elastin fiber network was observed near the anastomosis portion. Biotubes could thus be used as small-caliber vascular prostheses that greatly facilitate the healing process and exhibit excellent biocompatibility. © 2011 Wiley Periodicals, Inc. J Biomed Mater Res Part B: Appl Biomater 98B: 120–126, 2011.

Key Words: biotube, vascular grafts, autologous tissue, *in vivo* tissue engineering, connective tissue

INTRODUCTION

Therapies for coronary artery and peripheral vascular diseases often require replacement of damaged vessels with vascular grafts. For reconstruction of large-diameter arteries, such as the aorta or the iliac artery, vascular prostheses prepared from conventional synthetic biomaterials, such as expanded polytetrafluoroethylene (ePTFE) or poly (ethylene terephthalate) (Dacron), are used satisfactorily. However, these synthetic biomaterials are clinically unacceptable for reconstruction of small-diameter (internal diameter of <5 mm) arteries, which is required in lower-extremity bypass and coronary artery bypass grafting procedures, due to thrombosis, limited reendothelialization, and neointimal hyperplasia, owing mainly to the inherent properties of the synthetic biomaterials. Therefore, physicians routinely use autologous arterial (e.g., internal thoracic artery and radial artery) or venous (e.g., saphenous vein) grafts for such reconstruction procedures.[1,2] Unfortunately, the number of appropriate vessels is limited in many patients due to coexisting diseases, size mismatches, or previous procedures. Thus, the development of innovative technologies targeting the fabrication of small-caliber vascular grafts is imperative.

Recently, a novel and practical concept in regenerative medicine known as in-body tissue architecture technology, based on the tissue-encapsulation phenomenon in living bodies, has been implemented for the development of autologous tissues for implantation.[3–8] This phenomenon is a biological defense mechanism and involves the embedding of foreign bodies made of certain synthetic materials into body tissues. In-body tissue architecture technology has the following advantages: (1) the prostheses induce no immunological rejection, (2) the materials are nontoxic and biocompatible, and (3) the prostheses may adapt as the recipients grow. In addition, tissue prostheses can be fabricated in a wide range of shapes and sizes to suit each individual recipient. Most importantly, neither complex *in vitro* cell management nor a specialized clean laboratory facility is required, both of which are time-consuming and expensive. We previously developed an in-body tissue architecture-based,

Correspondence to: K. Kanda; e-mail: kei@koto.kpu-m.ac.jp or Y. Nakayama; e-mail: nakayama@ri.ncvc.go.jp
Contract grant sponsor: Ministry of Education, Culture, Sports, Science and Technology of Japan; contract grant number: B21360123

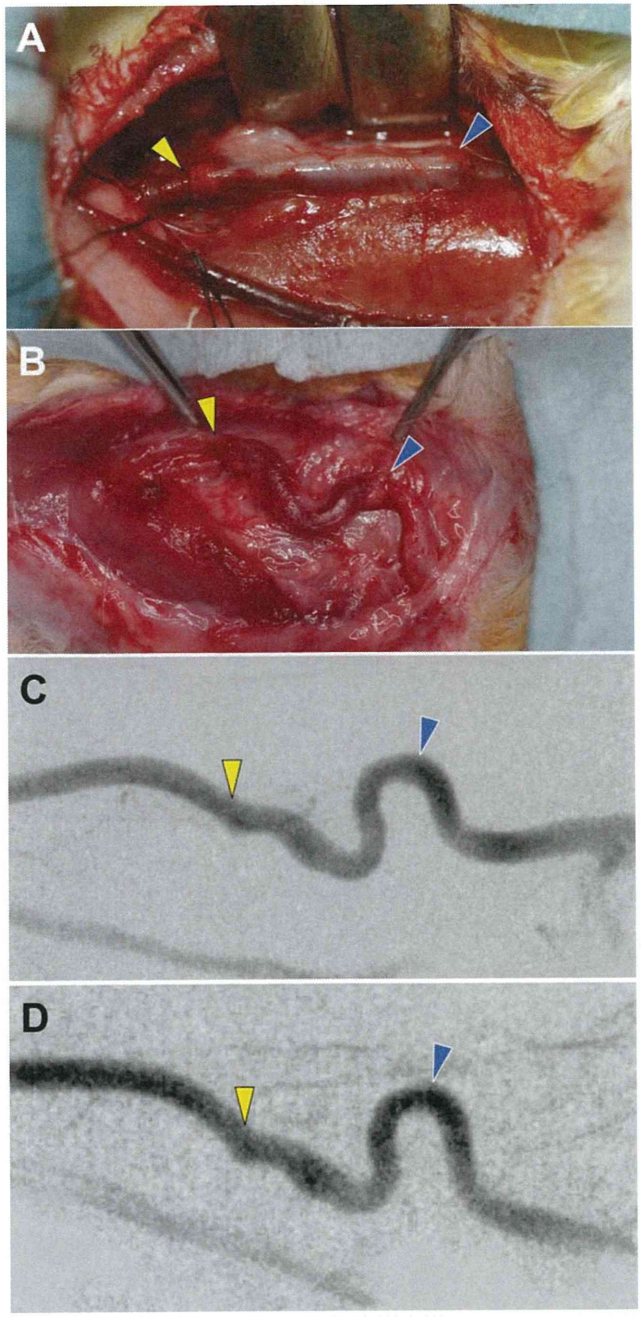

FIGURE 1. Macroscopic photograph of a biotube immediately (A) and 26 months (B) after implantation in the carotid artery of a rabbit. Angiographic scan after 17 months (C) and 26 months (D) after implantation. The arrows show the anastomosis portion (yellow: proximal side; blue: distal side). [Color figure can be viewed in the online

small-caliber vascular grafts termed as "biotubes"[3–5] that did not require *in vitro* pretreatment with cell seeding but showed dense collagen fibers with regular circumferential orientation and few elastin fibers without significant neointimal thickening for up to 3 months after implantation in rabbits.[5]

In this study, a small-caliber, biotube vascular graft was autoimplanted in a rabbit for 26 months. Long-term morphogenetic and mechanical changes in vascular wall regeneration were investigated in detail using a limited, but valuable example with comparison with the previous acute-term implantation study up to 3 months.[5]

MATERIALS AND METHODS

Preparation and implantation of biotubes

Two Japanese white rabbits (weighing ca. 2 kg) were used in this experiment, and they were treated humanely according to the Principles of Laboratory Animal Care (National Institutes of Health Publication No. 56-23; received in 1985). The research protocol for this study (No. 9044) was approved by the ethics committee of the National Cerebral and Cardiovascular Center Research Institute. Anesthesia was induced by intramuscular injection of a mixture of ketamine (62.5 mg/kg) and xylazine (8.3 mg/kg) and maintained by bolus intramuscular injection of a quarter of the initial doses. The molds, prepared by covering a silicone rod (diameter, 3 mm; length, 30 mm) at both ends with two pieces of microporous sponge tubes (length of the sponge, 3 mm; internal and external diameters, 3 and 5 mm, respectively; size of micropores, 100–150 μm)[4] were placed into the dorsal subcutaneous pouches of the rabbits; after 2 months, the implants were harvested before carotid transplantation. Six biotubes were obtained from the implant after trimming the peripheral connective tissues and extracting the rod. One of the obtained biotubes was loaded with argatroban (1 mg/graft, Mitsubishi Chemical Co., Tokyo, Japan) before autoimplantation. The other five biotubes were used for histological or mechanical evaluations.

A paratracheal incision was made along the trachea and the common carotid artery was dissected, yielding a segment ~ 5 cm in length. After intravenous injection of heparin (Novo Heparin, Novo Nordisk Pharmaceuticals, Copenhagen, Denmark: 100 U/kg), the artery was cross-clamped 20 mm away from the anastomoses and a segment 30-mm long was resected. The biotube was interposed to the same rabbit by means of end-to-end anastomosis. The anastomosis was constructed using eight interrupted 9–0 polypropylene sutures by simple interrupted stitch under microscopic guidance on each side, and the outer tube that was placed outside of the inner tube over the anastomosis was roughly fixed to the adventitia of the adjacent native artery. Neither antiplatelet nor anticoagulant agents were administered, except for the intraoperative heparin injection. Follow-up angiography was performed at 17 and 26 months after implantation. The harvested biotube was divided into three longitudinal specimens. Two specimens from the proximal and midportions were used for histological examination at the longitudinal and circumferential directions, respectively, and the other specimen at the distal portion was used for evaluation of mechanical properties.

Histological examination

Two specimens were fixed in a 10% formalin solution (pH 7.4), dehydrated with alcohol series, and embedded in paraffin. The tissues were cut into 3- to 5-μm thick sections and stained with hematoxylin and eosin. In addition, the histological sections were stained with Sirius red for estimating the density and orientation of collagen or with Elastica van

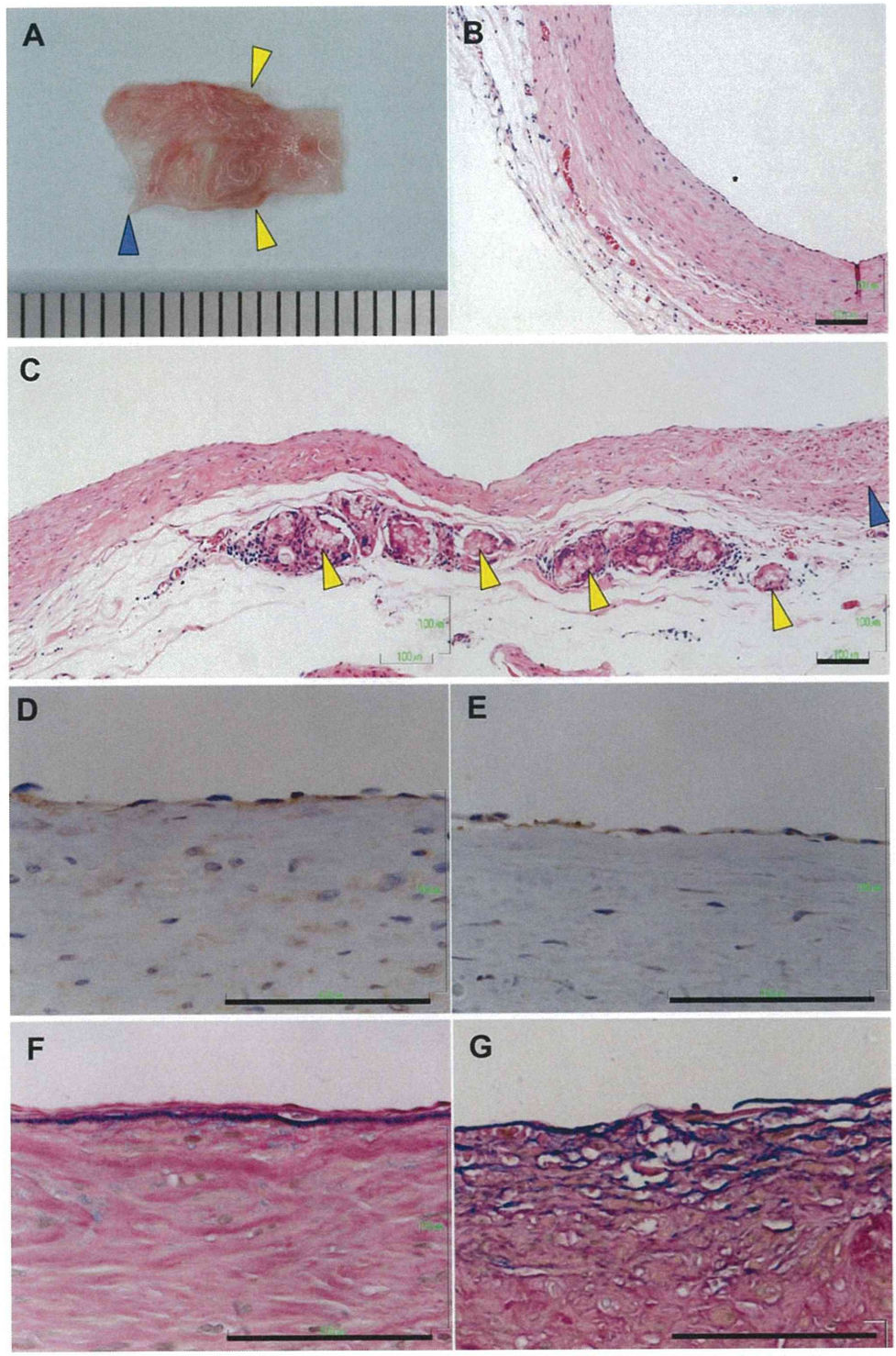

FIGURE 2. (A) Macroscopic photograph of the luminal surface of the distal half of the harvested biotube. The yellow arrows show the anastomosis portion on the distal side. The blue arrow shows the midportion. Histological photographs of the harvested biotube stained with hematoxylin and eosin at the midportion in a circumferential direction (B) and the distal anastomosis portion in a longitudinal direction (C). The blue arrow shows the distal anastomosis portion, and the yellow arrows show the degraded polyurethane cuffs used for reinforcement. Immunohistological staining for platelet endothelial cell adhesion molecule 1 (PECAM-1) at the midportion (D) and the proximal anastomosis portion (E). Elastica van Gieson staining at the midportion (F) and the proximal anastomosis portion (G). Bar = 100 μm. [Color figure can be viewed in the online

Gieson for estimating the same of elastin. Immunohistochemistry was performed using monoclonal antibodies against platelet-endothelial cell adhesion molecule (PECAM-1; Dako Japan, Kyoto, Japan; 1:100 dilution) and α-smooth muscle actin (α-SMA; Dako Japan; 1:100 dilution). The sections were treated with 0.3% H_2O_2 for 20 min to inhibit